Article

Convective Rolls and Hydrothermal Waves in Evaporating Sessile Drops

George Karapetsas,[†] Omar K. Matar,*,[†] Prashant Valluri,[‡] and Khellil Sefiane[‡]

[†]Department of Chemical Engineering, Imperial College London, London SW7 2AZ, U.K.
[‡]School of Engineering, The University of Edinburgh, Edinburgh EH9 3JL, U.K.

ABSTRACT: Recent experiments on the evaporation of sessile droplets have revealed the spontaneous formation of various patterns including the presence of hydrothermal waves. These waves had previously been observed, in the absence of evaporation, in thin liquid layers subjected to an imposed, uniform temperature gradient. This is in contrast to the evaporating droplet case wherein these gradients arise naturally due to evaporation and are spatially and temporally varying. In the present paper, we present a theory of evaporating sessile droplets deposited on a heated surface and propose a candidate mechanism for the observed pattern formation using a linear stability analysis in the quasi-steady-state approximation. A qualitative agreement with experimental trends is observed.
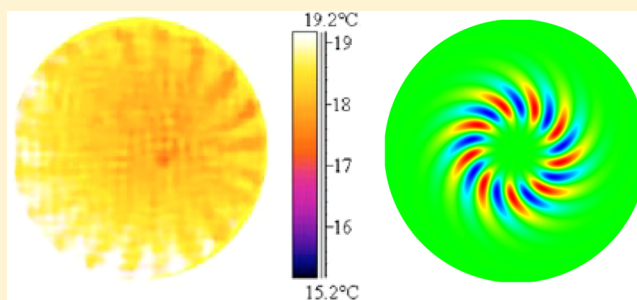
INTRODUCTION

The dynamics of evaporating droplets are central to several technological and biomedical applications that involve heat and mass transport; these include small-scale applications, such as cooling of microelectronics chips and medical diagnostics based on stain analyses of biofluid samples,[1,2] and industrial-scale applications, such as heat exchangers, boilers, and condensers. The behavior of these droplets, however, remains poorly understood, as demonstrated by recent experiments on the evaporation of sessile droplets that revealed the spontaneous formation of various patterns including the presence of hydrothermal waves (HTWs)[3] (see Figure 1). The latter correspond to thermally induced traveling waves, which occur in the absence of surface deformations, and derive their energy from the base flow temperature gradients. The experimental work of Sefiane et al.[3] on droplets evaporating under ambient conditions was also complemented by experiments performed on superheated substrates;[4] it was concluded that increasing the superheat tends to increase the wavenumber of the thermal waves. More recently, Brutin et al.[5] presented a series of experiments on heated droplets exhibiting similar patterns to those reported in Sefiane et al.[3]

In previous work, the presence of HTWs was predicted, in the absence of evaporation, for thin liquid layers of constant thickness subjected to an externally imposed, uniform temperature gradient.[6−8] Smith and Davis[6] have shown that fluid layers subjected to sufficiently large horizontal temperature gradients become unstable and exhibit steady longitudinal rolls or unsteady hydrothermal waves. The latter propagate parallel and almost perpendicularly to the temperature gradient for small and large Prandtl numbers, respectively.[6−8] The presence of these waves has been experimentally confirmed in differ-

entially heated pools of ethanol[9] and silicon oil.[10−12] In the case of annular pools, HTWs resemble spirals at relatively large values of the thickness, and, for films whose depth is less than the capillary length scale, the observed HTWs propagate radially from the inner to the outer edge of the cylinder. Temperature fluctuations associated with HTWs propagating in an annulus have also been reported;[13] the amplitude and frequency of these oscillations depend on the imposed temperature gradient as well as the fluid depth.

In contrast to the evaporation-free cases studied previously, the temperature gradients and the drop thickness in the case of evaporating droplets vary spatially and temporally, and are a natural consequence of the evaporation process; exploring their role in the formation of convective rolls and hydrothermal waves in evaporating droplets is the subject of the present work. We focus on heated droplets because this problem permits use of the simplifying "one-sided" approximation (negligible vapor density, viscosity, and thermal conductivity),[14] allowing us to concentrate solely on the liquid phase; this also allows us to derive the simplest model that contains the physical mechanisms that drive instability and pattern formation. We solve numerically for the evolving base state, corresponding to an evaporating, two-dimensional droplet, and then linearize about this state by invoking the quasi-steady-state approximation to investigate its linear stability characteristics to azimuthal perturbations. Our results demonstrate that the "one-sided" model is sufficient to describe the development of pattern formation in evaporating sessile droplets.
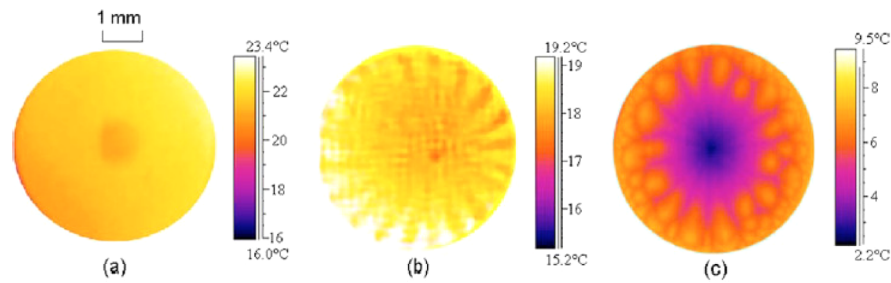
Figure 1. Patterns in sessile drops of water, methanol, and FC-72 refrigerant evaporating on silicon substrates, shown in panels a−c, respectively, obtained using IR thermography. Reprinted with permission from ref 3. Copyright 2008, American Institute of Physics.

■ PROBLEM FORMULATION

We study the behavior of an evaporating droplet of density ρ, viscosity μ, and thermal conductivity λ, which rests on a uniformly heated solid surface (see Figure 2). The substrate
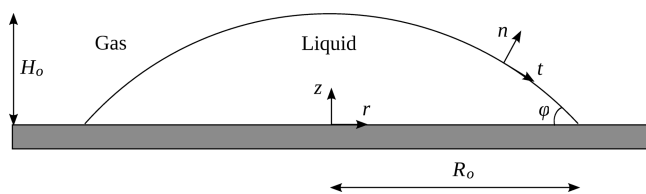

Figure 2. Schematic of an evaporating droplet on a solid surface.

temperature, T_w, is constant, while the surrounding temperature is T_a. The liquid−air interface has a surface tension, σ, which depends linearly on temperature, $\sigma = \sigma_0 - \gamma(T_s - T_a)$; T_s denotes the interfacial temperature, $\gamma = -d\sigma/dT$, and σ_0 is the surface tension at the ambient temperature. We assume that the droplet initially has maximal thickness H_0, radius R_0, and uniform temperature, $T|_{t=0} = T_w$, and adopt the "one-sided" model of evaporation (negligible vapor density, viscosity, and thermal conductivity).[14]

We introduce the following scaling (tildes denote dimensionless variables):

$$(\tilde{r}, \tilde{z}) = (r, z)/H_0, \quad \tilde{\mathbf{v}} = \mathbf{v}/U, \quad \tilde{P} = PH_0/(\mu U),$$

$$\tilde{T} = (T - T_a)/\Delta T, \quad \tilde{J} = JH_0 L/(\lambda \Delta T),$$

$$\tilde{\sigma} = \sigma/\sigma_0, \quad \tilde{t} = tU/H_0 \tag{1}$$

where $\varepsilon = H_0/R_0$, $\Delta T = T_w - T_a$, $U = \varepsilon\gamma\Delta T/\mu$ is a characteristic velocity, L is the latent heat, while $\mathbf{v}$, P, J, and t denote the velocity vector, pressure, evaporative flux, and time, respectively. The tildes are henceforth suppressed. The dimensionless groups that arise are the Reynolds number, $Re = \rho UH_0/\mu$, the Prandtl number, $Pr = \mu C_p/\lambda$, the Stokes number, $St = \rho g H_0^2/(\mu U)$, the effective Marangoni number, $Ma = \gamma\Delta T/\sigma_0$, and the evaporation number, $E = \lambda\Delta T/(\rho UH_0 L)$; the evaporation number represents the ratio of the viscous to evaporative time scales. Table 1 provides the properties of fluids used in the experiments shown in Figure 1 and the corresponding values of the dimensionless parameters.

The flow in the droplet is incompressible and governed by the following dimensionless mass, momentum, and energy balance equations

$$\nabla \cdot \mathbf{v} = 0 \tag{2}$$

$$Re\left(\frac{\partial \mathbf{v}}{\partial t} + \mathbf{v} \cdot \nabla \mathbf{v}\right) + \nabla P - \nabla^2 \mathbf{v} - St\,\mathbf{g} = 0 \tag{3}$$

Table 1. Physical Properties and Dimensionless Numbers of fluids at 25 °C and 1 atm[a]

	water	methanol	FC-72
ρ (kg m^{-3})	997	791	1680
ρ_g (kg m^{-3})	0.59	0.21	4.35
μ (mPa s)	0.890	0.560	0.638
λ (W m^2 K^{-1})	0.606	0.203	0.057
C_p (J kg^{-1} K^{-1})	4180	2531	1100
L (kJ kg^{-1})	2449	1165	88
σ_0 (mN m^{-1})	72.7	22.7	12.0
γ (mN m^{-1} K^{-1})	0.17	0.08	0.09
Re	128	121	223
Pr	6.14	6.98	12.3
Ma	0.012	0.018	0.037
E	1.1×10^{-5}	1.3×10^{-5}	2.3×10^{-5}
St	20.7	34.9	65.8
K	7.9×10^{-5}	2.4×10^{-5}	1.8×10^{-5}

[a]The dimensionless parameters are evaluated assuming $\Delta T = 5$ °C and a droplet with initial radius $R_0 = 3$ mm and maximum height $H_0 = 0.6$ mm.

$$RePr\left(\frac{\partial T}{\partial t} + \mathbf{v} \cdot \nabla T\right) - \nabla^2 T = 0 \tag{4}$$

The boundary conditions imposed at the solid wall ($z = 0$) correspond to no-penetration, the Navier slip condition, and constant temperature:

$$v_z = 0 \tag{5}$$

$$\frac{\partial v_r}{\partial z} = \beta_{sl} v_r \tag{6}$$

$$T = 1 \tag{7}$$

Recently, Ren and E[15] performed molecular dynamics simulations to investigate the suitability of various boundary conditions along a moving contact line. Their simulations suggest that the best approach among the models they have studied is to replace the Navier slip condition at the contact line ($z = 0$, $r = R_c$) with the following equation

$$v_r = \beta_{cl}(\cos \phi_s - \cos \phi) \tag{8}$$

According to this model, the deviation of the dynamic contact angle, ϕ, from its static value, ϕ_s, provides the driving force for contact line motion. This model is very similar to the Cox−Voinov model,[16] widely used for thin drops using the lubrication approximation, but is more suitable for drops that are not so thin.

Along the liquid–air interface, we impose a local stress balance, neglecting the effect of vapor recoil

$$\mathbf{n}\cdot(-PI + \nabla\mathbf{v} + \nabla\mathbf{v}^T) - \varepsilon^{-1}Ma^{-1}(\nabla_s\sigma + 2\mathcal{H}\mathbf{n}\sigma) = 0 \tag{9}$$

where $2\mathcal{H} = -\nabla_s\cdot\mathbf{n}$, $\nabla_s = (I - \mathbf{nn})\nabla$ and I is the identity matrix. In addition, we impose the kinematic equation

$$\partial f/\partial t + \mathbf{v}\cdot\nabla f = EJ \tag{10}$$

where f describes the position of the interface and a condition for thermal flux

$$J = -\mathbf{n}\cdot\nabla T \tag{11}$$

The evaporative effects are modeled using the following constitutive equation.[14]

$$KJ = T_s \tag{12}$$

The parameter $K = \lambda T_a^{3/2}(2\pi R_g)^{1/2}/(\rho_g H_0 L^2)$ measures the degree of nonequilibrium at the evaporating interface; ρ_g and R_g denote the vapor density and gas constant, respectively. In the results that will be presented below, we have taken the value of K to be larger than that shown in Table 1 for demonstration purposes. However, we should note that the value of K can be associated with the inverse of the Biot number used by Ehrhard and Davis[17] and therefore a wider range of K can be relevant for these systems.

The governing equations are discretized using the finite-element method combined with an elliptic mesh generation scheme, which is capable of following the deformations of the physical domain.[18] For all the computations presented in this paper, we have used 100 and 20 elements in the radial and axial direction, respectively; convergence was achieved upon mesh refinement. The resulting set of discrete equations is integrated in time with the implicit Euler method.

Linear Stability Analysis. In order to examine the stability of the flow, we consider the effects of infinitesimal disturbances to the base flow and perform a linear stability analysis. We apply the quasi-steady-state approximation (QSSA) which assumes that the growth rate of the disturbances is much faster than the rate of change of the evolving base state. Accordingly, we "freeze" the solution at one time instant, t_{qs}, and use this solution as the base state about which we perform a linear stability analysis. We perturb this base state solution allowing for 3D disturbances and write each variable in the following form

$$X(r, \theta, z, t) = X_b(r, z, t_{qs}) + X_p(r, z)e^{\alpha t + ik\theta} \tag{13}$$

where X_b is the "frozen" base state solution and X_p is the perturbation. Substituting these normal modes into the governing equations and neglecting higher-order terms, we obtain a generalized eigenvalue problem of the form

$$P\mathbf{x} = \alpha Q\mathbf{x} \tag{14}$$

where α are the eigenvalues and x the eigenvectors. Regarding the boundary conditions at the axis of symmetry, we follow a similar approach to Preziosi et al.[19] The eigenvalue problem is solved using the Arnoldi algorithm as it is implemented in the ARPACK library.

■ RESULTS

Base State. We will begin our study by considering first the case of an axisymmetric droplet. It is important to note that

inclusion of inertia, which has been largely ignored in previous studies,[20−22] makes this case quite novel. The presence of inertia may give rise to interesting phenomena such as interfacial oscillations,[23] which will be discussed below.

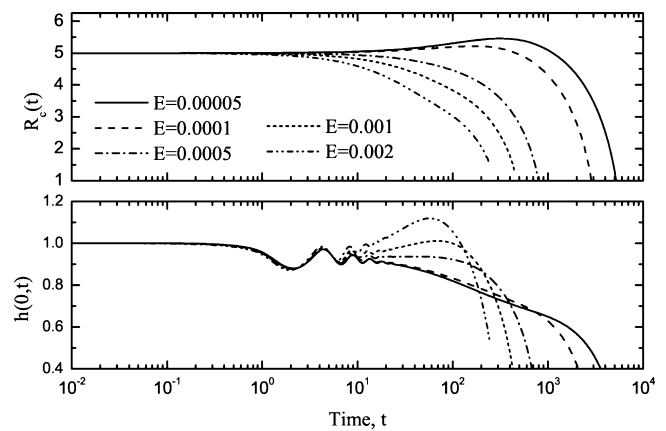Figure 3 presents simulations for various values of the evaporation number, E, while the rest of the parameters are

Figure 3. Time evolution of the position of the contact line, R_c, and the height of the air–liquid interface at $r = 0$, $h(0, t)$, for $Re = 100$, $Pr = 1$, $St = 50$, $Ma = 0.01$, $K = 0.1$, $\beta_{sl} = 10^5$, $\phi_s = 0.2$, $\beta_{cl} = 0.1$, and $\varepsilon = 0.2$.

shown in the caption of the same figure; the choices of the parameters used are in the range expected for small droplets of liquids like the ones used in the experiments of Figure 1. During the early stages of the simulation, the contact line remains pinned until at some point it starts receding due to droplet evaporation; the receding takes place earlier as E increases. Depending on the value of the static contact angle, and in cases where the evaporation is not too strong, the droplet may spread before it starts receding (e.g., for $E = 0.00005$). In Figure 3, we also present the time evolution of the droplet height at the axis of symmetry. Due to the presence of inertia, the liquid–air interface at some point starts to oscillate near the center of the drop and these oscillations soon decay; the amplitude and frequency of these oscillations are largely insensitive to E. On the contrary, they depend strongly on Re, and for very small values of Re, they become imperceptibly small (see Figure 4). Following the decay of these oscillations, the height of the droplet near the center may either decrease monotonically with time, for small values of E, or increase followed by rapid decrease, for large E. In the latter case, strong evaporation gives rise to steeper temperature gradients which induce, in turn, higher Marangoni stresses drawing fluid toward the center of the drop. With increasing time, the droplet loses
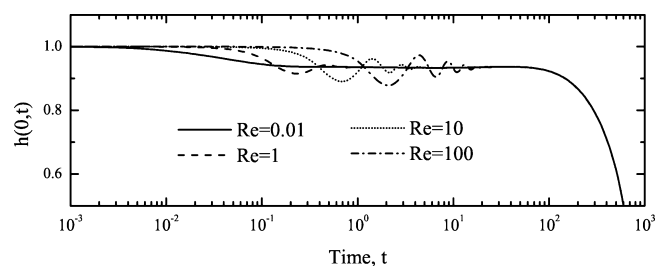

Figure 4. Time evolution of the height of the air–liquid interface at $r = 0$, $h(0, t)$, for various Re; the rest of the parameters are the same as in Figure 3.

mass due to evaporation, and the interfacial height decreases until the droplet vanishes.

Figure 5 depicts contour lines of the temperature field along with streamlines for $E = 0.0005$ at two different time instants,
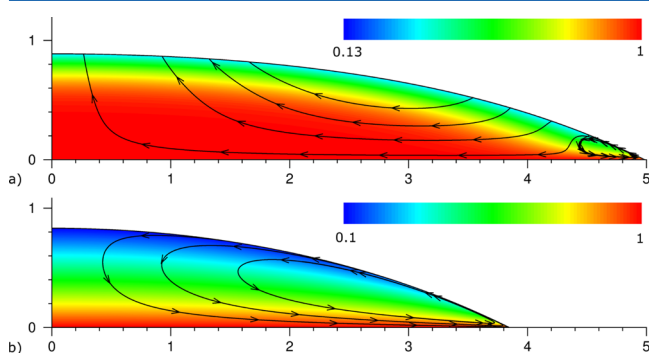

Figure 5. Contour plots of temperature and streamlines for $Re = 100$, $Pr = 1$, and $E = 0.0005$ at (a) $t_{qs} = 2.5$ and (b) $t_{qs} = 250$; the rest of the parameters are the same as in Figure 3. A video of the simulation is available at http://workspace.imperial.ac.uk/ceFluidMechanics/Public/Re100_Pe100_E0.0005.avi.

keeping the rest of the parameters fixed. At early times, the temperature decreases locally around the liquid−air interface as the liquid cools due to evaporation and another temperature gradient arises close to the contact line due to the presence of the heated solid wall, which is at constant temperature, higher than the saturation temperature. The temperature gradient in the contact line region induces locally high Marangoni stresses, which give rise to a small recirculation vortex. With increasing time, the temperature gradient spreads along a larger portion of the interface and the vortex grows significantly until it engulfs the whole droplet; the direction of the vortex is in agreement with previous studies for substrates of infinite conductivity.[21,24] Increasing the value of Pr renders the dynamics more complex and, as can be seen in Figure 6, for $Pr = 7$, multiple rolls are
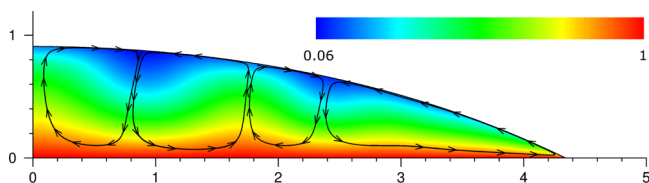

Figure 6. Contour plots of temperature and streamlines for $Re = 20$, $Pr = 7$, and $E = 0.0005$ at $t_{qs} = 125$; the rest of the parameters are the same as in Figure 3. A video of the simulation is available at http://workspace.imperial.ac.uk/ceFluidMechanics/Public/Re20_Pe140_E0.0005.avi.

formed; increasing the value of Pr leads to an increase in the number of these cells. Furthermore, their number and size decreases with time as the droplet shrinks due to evaporation. We should note that the flow in this case is similar to the cellular motion described by Pearson[25] due to surface tension forces when a thin layer of fluid is heated from below, in the absence of buoyancy.

Linear Stability Analysis. We proceed in our analysis by performing a quasi-steady-state linear stability analysis as described in section 2 to account for nonaxisymmetric perturbations. We compute the eigenvalues of our system for various values of the wavenumber, k. The stability of the flow is

determined by the real part of the eigenvalues, α. When all the eigenvalues have a negative real part, the corresponding eigenmodes will decay, whereas if at least one eigenvalue has a positive real part the corresponding eigenmode is linearly unstable.

In Figure 7, we present the computed eigenvalues of the most dangerous modes as a function of the base state time for $E = 0.0005$, keeping the rest of parameters the same as in Figure 3; α_R and α_I denote the real and imaginary parts of the eigenvalue, respectively. Every point of this figure corresponds to a solution of an eigenvalue problem, as described above, assuming that at the corresponding time instant the base state is quasi-steady. The solid line in Figure 7a depicts the evolution of dh/dt at $r = 0$. The rest of the subplots in this figure present the wavenumber associated with the most unstable mode, k_d, and the cutoff mode, k_c, beyond which all modes are stable. At early times, the computed eigenvalues are affected significantly by the presence of surface deflections, which are due to the presence of inertia. These results indicate that the validity of the QSSA analysis is questionable at early times because the presence of interfacial oscillations makes the growth rate of the base state comparable to that of the perturbation. However, after some time, the base state oscillations decay and the perturbation growth rates become much larger than that of the base state. Since the perturbations grow exponentially with time, we can safely assume that the QSSA analysis becomes valid after this point (approximately for $t > 20$ for this choice of parameters).

In Figure 8a,b, we show contour plots of the temperature disturbances in (r, θ) that correspond to the most dangerous mode at two "quasi-static" times with $Re = 100$ and $Pr = 1$. Inspection of this figure shows that, for times beyond which the QSSA is valid (see Figure 7), the most dangerous eigenvalues have zero imaginary part, indicating the presence of stationary rolls. Also, the growth rate and the value of the wavenumber associated with the most dangerous mode decrease with time, as the droplet evaporates, in direct agreement with the experimental observations.[3] Although the validity of the QSSA analysis at early times is questionable, as noted above, it is still interesting to examine the form of the eigenvectors at times where the base state growth rate is relatively small. We observe that modes with nonzero imaginary parts emerge and this is the signature of traveling waves in the azimuthal direction. The presence of these hydrothermal waves can be seen clearly in Figure 8a. It is noteworthy that these wave-trains resemble remarkably the ones seen in the experiments[3] (see Figure 1b). For $20 < t < 50$, the most dangerous mode has $k = 3$, and the temperature contours associated with this mode, shown in Figure 8b, are reminiscent of the "flower-like" patterns observed in differentially heated cylindrical cavities.[12] In Figure 8c, we present the selected mode for the base state shown in Figure 6, generated for relatively late times, $t = 125$, $Re = 20$, and $Pr = 7$. In this case, the most dangerous mode has $k = 6$. The base flow in combination with the perturbation profile shown in Figure 8c results in patterns which resemble the experimental observations in Figure 1c for FC-72.

In order to identify the physical mechanism and the nature of unstable modes, we have performed an "energy budget" analysis following the methodology outlined in the Appendix. The analysis was performed for the cases shown in Figure 8, and the terms with the largest contributions to the budget are given in Tables 2 and 3; the ones omitted are either zero or negligible. The energy decomposition reveals that the dissipative terms, ϕ_{dis} and ϕ_{dif}, provide negative contributions;
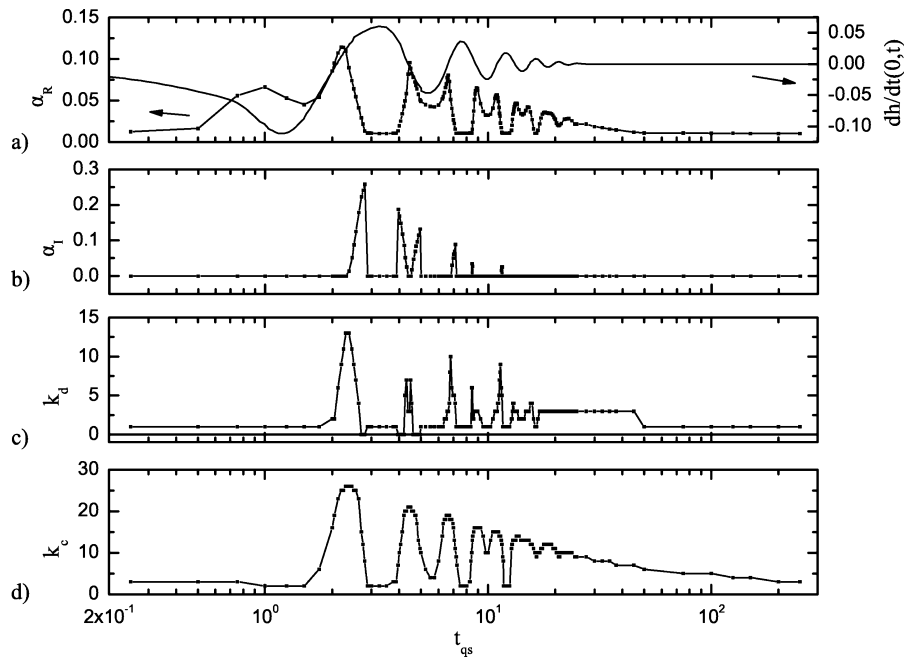
Figure 7. Evolution of the most unstable mode as predicted by the QSSA analysis for $E = 0.0005$; the rest of the parameters are the same as in Figure 3.

k=9, α=0.064+0.088i   k=3, α=0.022   k=6, α=0.145

a) Re=100, Pr=1, t=2.5   b) Re=100, Pr=1, t=25   c) Re=20, Pr=7, t=125
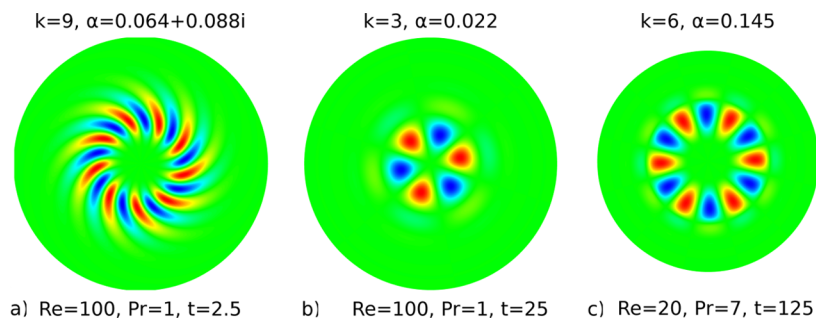
Figure 8. Contour plots of the temperature perturbations of the most unstable modes for $E = 0.0005$; the rest of the parameters are the same as in Figure 3.

Table 2. Kinetic Energy Budgets for the Cases Shown in Figure 8, Calculated Using eq 15

Re	Pr	t	k_d	ϕ_{rey}	ϕ_{dis}	$\phi_{int,1}$
100	1	2.5	9	-6.03×10^{-3}	-1.06×10^{-1}	1.14×10^{-1}
100	1	25	3	-1.97×10^{-7}	-2.41×10^{-5}	2.51×10^{-5}
20	7	125	6	-1.13×10^{-4}	-1.90×10^{-3}	1.95×10^{-3}

Table 3. Thermal Energy Budgets for the Cases Shown in Figure 8, Calculated Using eq 16

Re	Pr	t	k_d	ϕ_{adv}	ϕ_{dif}	$\phi_{int,2}$
100	1	2.5	9	1.31×10^{-1}	-1.09×10^{-1}	-1.83×10^{-2}
100	1	25	3	6.29×10^{-5}	-5.27×10^{-5}	-6.67×10^{-6}
20	7	125	6	5.28×10^{-3}	-2.88×10^{-3}	-5.97×10^{-4}

this indicates that viscous dissipation and thermal diffusion provide a restoring effect and are stabilizing, as expected. The only positive contributions to dKE/dt and dTE/dt come from $\phi_{int,1}$ and ϕ_{adv}, respectively. This implies that the unstable modes are driven by Marangoni stresses and advection. These results demonstrate that the instabilities presented in this paper share a similar mechanism to that which drives the formation of hydrothermal waves. This mechanism is described in detail by Smith and Davis[6−8] for thin liquid layers of constant thickness

subjected to an externally imposed, uniform temperature gradient: for small Pr number, it involves the transfer of energy from the horizontal basic state temperature field to the disturbances through horizontal convection, whereas, for large Pr number, it involves the transfer of energy from the vertical basic state temperature field to the disturbances through vertical convection. It is important to reiterate that an important difference in the present case is the fact that the temperature gradients which drive this instability are not

imposed externally but are a natural consequence of the evaporating process.

The role of evaporation on the stability of the flow considered in the present paper is quite complex: on the one hand, it stabilizes the flow by removing heat from the interface with a tendency to make the temperature along the interface more uniform; on the other hand, it destabilizes it by inducing higher thermal gradients in the radial direction due to the presence of the solid wall. This interplay is demonstrated by the fact that the term associated with Marangoni stresses, $\phi_{\text{int,1}}$, is positive and the term associated with the cooling effect of evaporation, $\phi_{\text{int,2}}$, is negative. By increasing the rate of evaporation, it is expected that the temperature will be more uniform along the interface, closer to the saturation temperature, and therefore, its stabilizing role should prevail. The latter is supported by the results of our simulations shown in Figure 9. In this figure, we plot the dispersion curves for two different
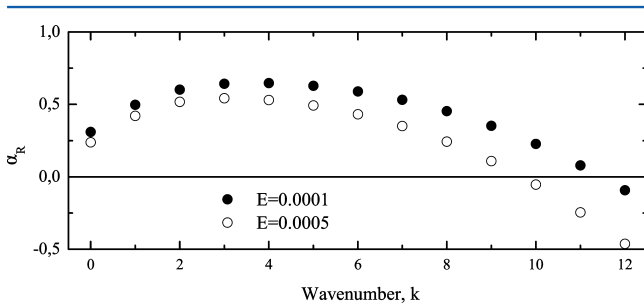

Figure 9. Dispersion curves for $Re = 100$ and $Pr = 1$ at $t = 25$ for different values of the evaporation number, E; the rest of the parameters are the same as in Figure 3.

evaporation numbers and we find that the wavenumber associated with the most unstable mode, k_d, decreases from $k_d = 4$ (for $E = 0.0001$) to $k_d = 3$ (for $E = 0.0005$). The trend is also similar for the cutoff mode, k_c, which decreases as the evaporation number, E, increases.

■ CONCLUSIONS

We have studied the dynamics of evaporating droplets on heated substrates using the "one-sided" model and focused on the instabilities that accompany the evaporation process. We have carried out a linear stability analysis of the flow in the quasi-steady-state approximation, which predicts the formation of stationary cells and traveling hydrothermal waves, in qualitative agreement with experimental observations. Furthermore, an "energy budget" decomposition highlighted the role of thermo-capillary-driven Marangoni stresses and advection as the key contributors to instability. To make a quantitative comparison with experimental observations, it would be necessary to proceed with three-dimensional (3D) dynamic simulations, since the flow in this case is inherently 3D. Moreover, it would also be useful to consider the more complicated, "two-sided" models[26−28] which should include the effect of vapor concentration taking into account the gaseous phase and the substrate thermal properties.

■ APPENDIX

The "energy" method considers the mean flow and the disturbance flow by evaluating the mechanical and thermal energy balance for the system. Decomposition of the kinetic and thermal energy equations into energy production and dissipation terms allows one to isolate the mechanisms by which energy is transferred from the base flow to the disturbances.

The disturbance kinetic and thermal energy equations are obtained by taking the inner product of the perturbed momentum and energy equation with the velocity and temperature perturbation, respectively. The resulting equations are integrated over the volume of the flow field and one periodic cycle in time (i.e., $0 < t < 2\pi/\alpha_I$). We end up with with the following equations:

$$\frac{d\text{KE}}{dt} = \phi_{\text{rey}} + \phi_{\text{dis}} + \phi_{\text{bnd,1}} \tag{15}$$

$$\frac{d\text{TE}}{dt} = \phi_{\text{adv}} + \phi_{\text{dif}} + \phi_{\text{bnd,2}} \tag{16}$$

where

$$\frac{d\text{KE}}{dt} = \frac{1}{2}\langle \mathbf{v}_p \cdot \mathbf{v}_p \rangle \tag{17}$$

$$\phi_{\text{rey}} = -\langle (\mathbf{v}_p \cdot \nabla \mathbf{v}_b + \mathbf{v}_b \cdot \nabla \mathbf{v}_p) \cdot \mathbf{v}_p \rangle \tag{18}$$

$$\phi_{\text{dis}} = -\frac{1}{Re}\langle (-P_p I + \nabla \mathbf{v}_p + (\nabla \mathbf{v}_p)^T) : \nabla \mathbf{v}_p \rangle \tag{19}$$

$$\phi_{\text{bnd,1}} = \frac{1}{Re}[\mathbf{n} \cdot (-P_p I + \nabla \mathbf{v}_p + (\nabla \mathbf{v}_p)^T) \cdot \mathbf{v}_p] \tag{20}$$

$$\frac{d\text{TE}}{dt} = \frac{1}{2}\langle T_p{}^2 \rangle \tag{21}$$

$$\phi_{\text{adv}} = -\langle (\mathbf{v}_p \cdot \nabla T_b + \mathbf{v}_b \cdot \nabla T_p) \cdot T_p \rangle \tag{22}$$

$$\phi_{\text{dif}} = -\frac{1}{RePr}\langle \nabla T_p \cdot \nabla T_p \rangle \tag{23}$$

$$\phi_{\text{bnd,2}} = \frac{1}{RePr}[(\mathbf{n} \cdot \nabla T_p)T_p] \tag{24}$$

The symbols $\langle \; \rangle$ and $[\;]$ are defined as follows:

$$\langle f \rangle = \int_0^{2\pi/\alpha_I} \int_V f \, dV \, dt \tag{25}$$

$$[f] = \int_0^{2\pi/\alpha_I} \int_S f \, dS \, dt \tag{26}$$

where V and S denote the drop volume and the surface area along the boundaries, respectively.

In eq 15, $d\text{KE}/dt$ denotes the rate of change of the kinetic energy of the disturbances, ϕ_{rey} represents the contribution of "Reynolds stress"-like terms (arising from the products of disturbances), ϕ_{dis} represents the viscous dissipation, and $\phi_{\text{bnd,1}}$ the contribution of stresses along the boundaries. In eq 16, $d\text{TE}/dt$ denotes the rate of change of the thermal energy of the disturbances, ϕ_{adv} represents the contribution of advection, ϕ_{dif} represents the thermal diffusion, and $\phi_{\text{bnd,2}}$ the contribution of thermal gradients along the boundaries. Both $\phi_{\text{bnd,1}}$ and $\phi_{\text{bnd,2}}$ can be decomposed into contributions associated with the interface and the wall

$$\phi_{\text{bnd},i} = \phi_{\text{int},i} + \phi_{\text{wall},i} \tag{27}$$

$\phi_{\text{int,1}}$ and $\phi_{\text{wall,1}}$ are evaluated using eq 20, where $S = S_{\text{int}}$ for $\phi_{\text{int,1}}$ and $S = S_{\text{wall}}$ for $\phi_{\text{wall,1}}$. Likewise, $\phi_{\text{int,2}}$ and $\phi_{\text{wall,2}}$ are evaluated using eq 24 along the interface and the wall,

respectively. The rest of the boundaries have no contribution to the energy budget.

■ AUTHOR INFORMATION

Corresponding Author
*E-mail: o.matar@imperial.ac.uk.

Notes
The authors declare no competing financial interest.

■ REFERENCES

(1) Sefiane, K. On the formation of regular patterns from drying droplets and their potential use for bio-medical applications. *J. Bionic Eng.* **2010**, *7*, S82−S93.

(2) Brutin, D.; Sobac, B.; Loquet, B.; Sampol, J. Pattern formation in drying drops of blood. *J. Fluid Mech.* **2011**, *667*, 85−95.

(3) Sefiane, K.; Moffat, J. R.; Matar, O. K.; Craster, R. V. Self-excited hydrothermal waves in evaporating sessile drops. *Appl. Phys. Lett.* **2008**, *93*, 074103.

(4) Sefiane, K.; Steinchen, A.; Moffat, R. On hydrothermal waves observed during evaporation of sessile droplets. *Colloids Surf., A* **2010**, *365*, 95−108.

(5) Brutin, D.; Sobac, B.; Rigollet, F.; Niliot, C. L. Infrared visualization of thermal motion inside a sessile drop deposited onto a heated surface. *Exp. Therm. Fluid Sci.* **2011**, *35*, 521−530.

(6) Smith, M. K.; Davis, S. H. Instabilities of dynamic thermocapillary liquid layers. Part 1. Convective instabilities. *J. Fluid Mech.* **1983**, *132*, 119−144.

(7) Smith, M. K. Instability mechanisms in dynamic thermocapillary liquid layers. *Phys. Fluids* **1986**, *29*, 3182.

(8) Davis, S. H. Thermocapillary instabilities. *Annu. Rev. Fluid Mech.* **1987**, *19*, 403.

(9) Schwabe, D.; Moeller, U.; Scheider, J.; Scharmann, A. Instabilities of shallow dynamic thermocapillary liquid layers. *Phys. Fluids A* **1992**, *4*, 2368.

(10) Riley, R. J.; Neitzel, G. P. Instability of thermocapillary−buoyancy convection in shallow layers. Part 1. Characterization of steady and oscillatory instabilities. *J. Fluid Mech.* **1998**, *359*, 143.

(11) Garnier, N.; Chiffaudel, A. Two dimensional hydrothermal waves in an extended cylindrical vessel. *Eur. Phys. J. B* **2001**, *19*, 87.

(12) Hoyas, S.; Mancho, A. M.; Herrero, H.; Garnier, N.; Chiffaudel, A. Benard-Marangoni convection in a differentially heated cylindrical cavity. *Phys. Fluids* **2005**, *17*, 054104.

(13) Schwabe, D.; Zebib, A.; Sim, B. C. Oscillatory thermocapillary convection in open cylindrical annuli. Part 1. Experiments under microgravity. *J. Fluid Mech.* **2003**, *491*, 239.

(14) Burelbach, J. P.; Bankoff, S. G.; Davis, S. H. Nonlinear stability of evaporating/condensing liquid films. *J. Fluid Mech.* **1988**, *195*, 463−494.

(15) Ren, W.; E, W. Boundary conditions for the moving contact line problem. *Phys. Fluids* **2007**, *19*, 022101.

(16) Bonn, D.; Eggers, J.; Indekeu, J.; Meunier, J.; Rolley, E. Wetting and spreading. *Rev. Mod. Phys.* **2009**, *81*, 739−805.

(17) Ehrhard, P.; Davis, S. H. Non-isothermal spreading of liquid drops on horizontal plates. *J. Fluid Mech.* **1991**, *229*, 365−388.

(18) Karapetsas, G.; Tsamopoulos, J. Transient squeeze flow of viscoplastic materials. *J. Non-Newtonian Fluid Mech.* **2006**, *133*, 35−56.

(19) Preziosi, L.; Chen, K.; Joseph, D. D. Lubricated pipelining: stability of core-annular flow. *J. Fluid Mech.* **1989**, *201*, 323−356.

(20) Hu, H.; Larson, R. G. Analysis of the microfluid flow in an evaporating sessile droplet. *Langmuir* **2005**, *21*, 3963−3971.

(21) Hu, H.; Larson, R. G. Analysis of the effect of Marangoni stresses on the microflow in an evaporating sessile droplet. *Langmuir* **2005**, *21*, 3972−3980.

(22) Bhardwaj, R.; Fang, X.; Attinger, D. Pattern formation during the evaporation of a colloidal nanoliter drop: a numerical and experimental study. *New J. Phys.* **2009**, *11*, 075020.

(23) Kavehpour, P.; Ovryn, B.; McKinley, G. H. Evaporatively-driven Marangoni instabilities of volatile liquid spreading on thermally conductive substrates. *Colloids Surf., A* **2002**, *206*, 409−423.

(24) Ristenpart, W. D.; Kim, P. G.; Domingues, C.; Wan, J.; Stone, H. A. Influence of substrate conductivity on circulation reversal in evaporating drops. *Phys. Rev. Lett.* **2007**, *99*, 234502.

(25) Pearson, J. R. On convection cells induced by surface tension. *J. Fluid Mech.* **1958**, *4*, 489−500.

(26) Sultan, E.; Boudaoud, A.; Ben Amar, M. Evaporation of a thin film: diffusion of the vapour and Marangoni instabilities. *J. Fluid Mech.* **2005**, *543*, 183−202.

(27) Sefiane, K.; Wilson, S. K.; David, S.; Dunn, G. J.; Duffy, B. R. On the effect of the atmosphere on the evaporation of sessile droplets of wate. *Phys. Fluids* **2009**, *21*, 062101.

(28) Dunn, G. J.; Wilson, S. K.; Duffy, B. R.; David, S.; Sefiane, K. The strong influence of substrate conductivity on droplet evaporation. *J. Fluid Mech.* **2009**, *623*, 329−351.